Radiation Physics and Chemistry 215 (2024) 111347

Contents lists available at ScienceDirect

Radiation Physics and Chemistry

journal homepage: www.elsevier.com/locate/radphyschem

Assessment of natural radioactivity and radon release potential of silurian black shales

Stefania DaPelo [a], Mirsina Mousavi Aghdam [b,d,*], Valentina Dentoni [b], Alfredo Loi [a], Paolo Randaccio [c], Quentin Crowley [d]

[a] Department of Chemical and Geological Sciences, University Campus of Monserrato, University of Cagliari, 09042, Cagliari, Italy
[b] Department of Civil and Environmental Engineering and Architecture, University of Cagliari, 09123, Cagliari, Italy
[c] Department of Physics, University Campus of Monserrato, University of Cagliari, 09042, Cagliari, Italy
[d] Department of Geology, School of Natural Sciences, Trinity College, D02PN40, Dublin, Ireland

ARTICLE INFO

Handling editor: Chris Chantler

Keywords:
Terrestrial radiation
Geogenic radon potential
Human exposure
Health risk

ABSTRACT

Many countries are developing a radon action plan to provide decision-makers with a reliable tool for reducing the harmful effects of radon exposure in dwellings and among the general public and, accordingly, to implement land development strategies. Mapping the geogenic radon release in different geological environments could assist in delineating areas that require priority monitoring and regulation, as well as applying radon reduction techniques in newly constructed buildings. In this paper, the activity concentration of ^{238}U, ^{226}Ra, ^{232}Th and ^{40}K and the exhalation rate of ^{222}Rn have been estimated for the Silurian black shales of Villasalto, a district in the south-eastern Sardinia (Italy). The radioactivity of ^{226}Ra, ^{232}Th and ^{40}K radionuclides was found relatively high (256.32 ± 87.00 Bq.kg^{-1}), low (44.16 ± 9.47 Bq.kg^{-1}) and moderate to high (856.28 ± 392.41 Bq.kg^{-1}) respectively. The *radon emanation coefficient* (E) and the *radon production rate* (P_{Rn}) have been calculated based on the analysis of the radon growth model inside a sealed chamber. E was found to correlate well with the activity concentration of ^{226}Ra, as well as with the grain size of the soil/rock samples under investigation. P_{Rn} was relatively high, ranging from 212.54 to 524.27 Bq.m^{-3}.h^{-1}. Furthermore, the mean value of the main radiation hazard indexes (i.e., the *radium equivalent activity*, the *outdoor gamma-ray dose rate* and the *annual effective dose*) were found to be 299.07 ± 138.62 Bq.kg^{-1}, 169.97 ± 75.58 nGy h^{-1} and 0.21 ± 0.09 mSv.y^{-1} respectively.

1. Introduction

The prevailing contribution to ionising radiation on the Earth's surface comes from natural sources: cosmic and terrestrial radiation, soil-gas radon (^{222}Rn) accumulated within indoor environments and natural radioactive elements contained in food and water (mainly potassium ^{40}K) (Baskaran, 2016; Chen et al., 2010; Dentoni et al., 2020; Aghdam and Mirsina, 2021; Mirsina Mousavi Aghdam et al., 2022; Zeeb et al., 2009). Secondary sources of ionising radiation include natural building materials and underground water. Among natural sources, soil-gas radon is by far the main contributor to human exposure and many epidemiological studies proved the incidence of cancer to be related to relatively low concentrations of gas radon and long-term exposure (Giustini et al., 2019; Darby et al., 2005; Bochicchio et al., 2019; Memarianfard et al., 2016); exposure conditions which may occur in homes, schools and working places (i.e. long time permanence within the day and possibly in a lifetime). The process of radon emanation, transport, and subsequent exhalation from the soil/bedrock to the Earth's surface is governed by many geological and meteorological variables (Coletti et al., 2022; Mostečak et al., 2018; Mirsina Mousavi Aghdam et al., 2023; Awan et al., 2022). The latter depends on the climate conditions, encompassing parameters like rainfall, surface wind, pressure, and air temperature (Baskaran, 2016; Abumurad and Al-Tamimi, 2001; Guagliardi et al., 2016). The geological features of lithogenic material and associated soils (i.e. depositional and geodynamic environment, and subsequent tectonic and weathering processes that may have occurred) significantly influence the concentration of radon-producing radionuclides in the Earth's crust (i.e. uranium concentration, since ^{222}Rn is a decay product of ^{238}U), as well as the soil/rock physical properties (grain size distribution, porosity and degree of rock fracturing). Hence, the assessment of the geological features that affect the exhalation of soil-gas radon into the air has gained

* Corresponding author. Department of Civil and Environmental Engineering and Architecture, University of Cagliari, 09123, Cagliari, Italy.
E-mail address: mousavim@tcd.ie (M.M. Aghdam).

https://doi.org/10.1016/j.radphyschem.2023.111347
Received 22 May 2023; Received in revised form 26 September 2023; Accepted 18 October 2023
Available online 23 October 2023

increasing interest, particularly in the development of the Geogenic Radon Potential (GRP) concept (Giustini et al., 2019; Coletti et al., 2022; Appleton and Miles, 2010; Mirsina Mousavi Aghdam et al., 2021; Olsthoorn et al., 2022; Tondeur et al., 2014).

Once radon has reached the Earth's surface (i.e. ground below foundations), it may penetrate indoor spaces through discontinuities and fractures in foundations or underground structures (Sadrnejhad et al., 2016; Aghdam and Mousavi, 2023; aldin Sadrnejhad et al., 2017). Additional anthropogenic factors may then favour indoor radon concentration (IRC), such as poor ambient ventilation and individual living habits. This results in markedly different IRC values even in neighbouring constructions with the same underlying geological formations (Giustini et al., 2019; Dardac et al., 2023; M.M. Aghdam et al., 2019). That is why direct methods (indoor radon sampling) are often used to identify *Radon Prone Areas* (RPAs), defined as *areas where the* ^{222}Rn *concentration exceeds a limit value of 300 Bq.m*$^{-3}$ *in more than 15% of the investigated houses* (EURATOM). While direct sampling of indoor radon effectively identifies RPAs, it fails in categorizing the role of geological and anthropogenic variables and does not contribute to estimating the amount of soil-gas ^{222}Rn delivered from nearby geological formations to the atmosphere (i.e.: *Geogenic Radon Potential*). On the other hand, indirect geological-based approaches, seek to infer the *Geogenic Radon Potential* (GRP) from the geological and geophysical information of the area under investigation. In that case, the subsequent estimation of IRC requires the definition of specific soil-indoor transfer factors (Kemski et al., 2009; Froňka, 2011). Several studies have discussed the correlation between IRC and GRP (Appleton et al., 2008; Kemski et al., 2009; Cinelli et al., 2017; Demoury et al., 2013; Yarmoshenko et al., 2016).

This study, following a geological-based approach, presents the result of in situ and laboratory measurements recently conducted to evaluate the natural radioactivity and radon emanation potential of the Silurian black shales of Villasalto, a district in south-eastern Sardinia (Italy). Black shales are in fact among the rocks that are recognised to contain high concentrations of radioactive elements and have been identified as a highly emitting source of radon in many parts of the world (Harrell et al. 1991; Harrell and McKenna, 1993; Soesoo and Hade, 2014). These sedimentary rocks contain organic carbon with anomalous enrichments in radioactive elements such as ^{238}U, ^{235}U, ^{40}K, and ^{232}Th, as well as trace elements like P, Mo, V, Se, Zn, and Hg (Ketris and Yudovich, 2009; Perry and I Marcellus Shale Team, 2011). The inorganic content can encompass various compositions such as clay, silt, sand, carbonate, chert, and phosphate (Ketris and Yudovich, 2009; Soesoo and Hade, 2014), and Uranium content varies in the interquartile range of 4–25 ppm, with carbonate black shale typically having lower values (10 $\pm$ 1.9 ppm) and clayey black shale higher values (14 $\pm$ 3 ppm) (Ketris and Yudovich, 2009). Uranium enrichment in black shales can occur due to deposition in anoxic environments (Swanson, 1961), like deep water as well as shallow environments (Baucon et al., 2020) where uranium is immobilized and concentrated. Additionally, subsequent metamorphic alterations can lead to the remobilization and re-concentration of uranium. The most extensive black shale deposits result from a two-phase process (Föllmi, 2012), observed in many Palaeozoic and Mesozoic strata worldwide. In Europe, the Estonian graptolite argillite and Swedish Alum shale provide examples of uranium deposition stemming from oceanic anoxic events (Soesoo and Hade, 2014). The rapid deglaciation of the late Hirnantian led to a sudden rise in sea level (Ghienne et al., 2014) triggering widespread post-glacial marine anoxia at the Silurian's onset (Corradini and Ferretti, 2009). Prominent sections of graptolite-rich black "schists", prevalent in the Landovery and Wenlock stages around peri-Gondwana in Europe, are found in Spain, Portugal, Sardinia, the Carnic Alps, Thuringia and Bohemia (Heckel, 2008; Gnoli et al., 2009). Similar phenomena led to the shale deposition of the late Pennsylvanian Midcontinent Sea, a large epeiric sea that covered a vast expanse in the United States (Algeo and Tribovillard, 2009).

As previously mentioned, this study discusses the result of in situ and laboratory tests performed on the Silurian black shales of Villasalto. In-situ gamma-ray spectrometry techniques were employed to estimate the natural radioactivity of the surveyed area. Seventeen samples of highly deformed Silurian black shales were collected from six selected sites. The concentration growth inside a sealed chamber has been modelled for each sample to calculate the e *radon emanation coefficient* (E). The correlation between the *radon emanation coefficient* and the main influencing variables has been investigated with *Pearson's matrix,* a measure of association between ordered pairs of continuous measurements from two groups (Pearson, 1895). The main *radiological hazard indexes* were also estimated for the test sites under investigation. The experimental findings hereby reported provide an overlook of the natural radioactivity of the Silurian black shales in south-eastern Sardinia and may contribute significantly to the elaboration of an accurate GRP map of the region.

1.1. Geology of the study area

The area under examination encompasses the abandoned *Su Suergiu mine* and the villages of Villasalto and Armungia in south-eastern Sardinia (Fig. 1). In this region, there are exposed low-grade metamorphic rocks of the Palaeozoic age that belong to the 'Nappe Zone' of the tectonic stacking of the Variscan Orogeny (Carmignani et al., 2001; Cocco et al., 2018, 2023). This area is characterized by thrusts and folds produced by the Variscan collision (lower Carboniferous) as well as the preceding lower Ordovician deformation phase known as the Sardic Phase (Cocco et al., 2018). The outcropping succession (Loi et al., 2023) consists of Cambrian to Lower Ordovician siliciclastic deposits, mainly shales, foliated micaceous sandstones, followed by Middle and Upper Ordovician volcanic arc rocks and Upper Ordovician siliciclastic deposits of the post-Sardic succession. The following Silurian and Devonian deposits comprise mainly black shales, lidites and limestones with argillites and marls interbedded, and successively covered by lower Carboniferous deposits of the Culm type (Barca et al., 2005). Black shales in Sardinia are mainly represented in Silurian formations and are similar to those cropping out in Thuringia and Bohemia (Barca et al., 2005; Gnoli et al., 2009). The most complete and best-known Silurian succession of southeastern Sardinia is exposed in the Gerrei tectonic Unit (Carmignani et al., 2001). The Silurian succession comprises two main levels lower and upper Graptolitic Shales, separated by a nodular calcareous unit (Ockerkalk). Upper Graptolitic shales document the lower Devonian (Corradini and Ferretti, 2009). The deposition of these shales took place in a reducing euxinic sapropelitic basin and then they were deeply folded and faulted during the Variscan tectonic evolution (Baucon et al., 2020). A cataclastic-mylonitic belt, derived from the Silurian and lower Devonian rocks, occurs in connection with the "Villasalto overthrust" (Carmignani et al., 2001) hosting mesothermal mineralization, which was extensively exploited underground from 1880 to 1960 (Cidu et al., 2014). Evidence of past mining activities includes the deposits of tailings and concentrated milled black shale gangue, as well as a network of mine tunnels, which pass through the Silurian succession. Tectonic structures, mine tunnels and deposits or dumps of small grain-size materials currently provide a privileged way for radon to escape toward the surface. Fig. 1 displays the modified and simplified version of the geological map of the Villasalto area, together with the location of the test sites under investigation and the sampling points. Wherever there was evidence of outcrops and cataclastic-mylonitic facies of black shales, a test site was identified. The samples (soil/rock) were collected from freshly broken surfaces. Fig. 2 shows the Silurian black shales of the Suergiu and the immediate surroundings.

2. Materials and methods

2.1. In-situ gamma-ray spectrometry

In an attempt to map the distribution of natural radioactivity within

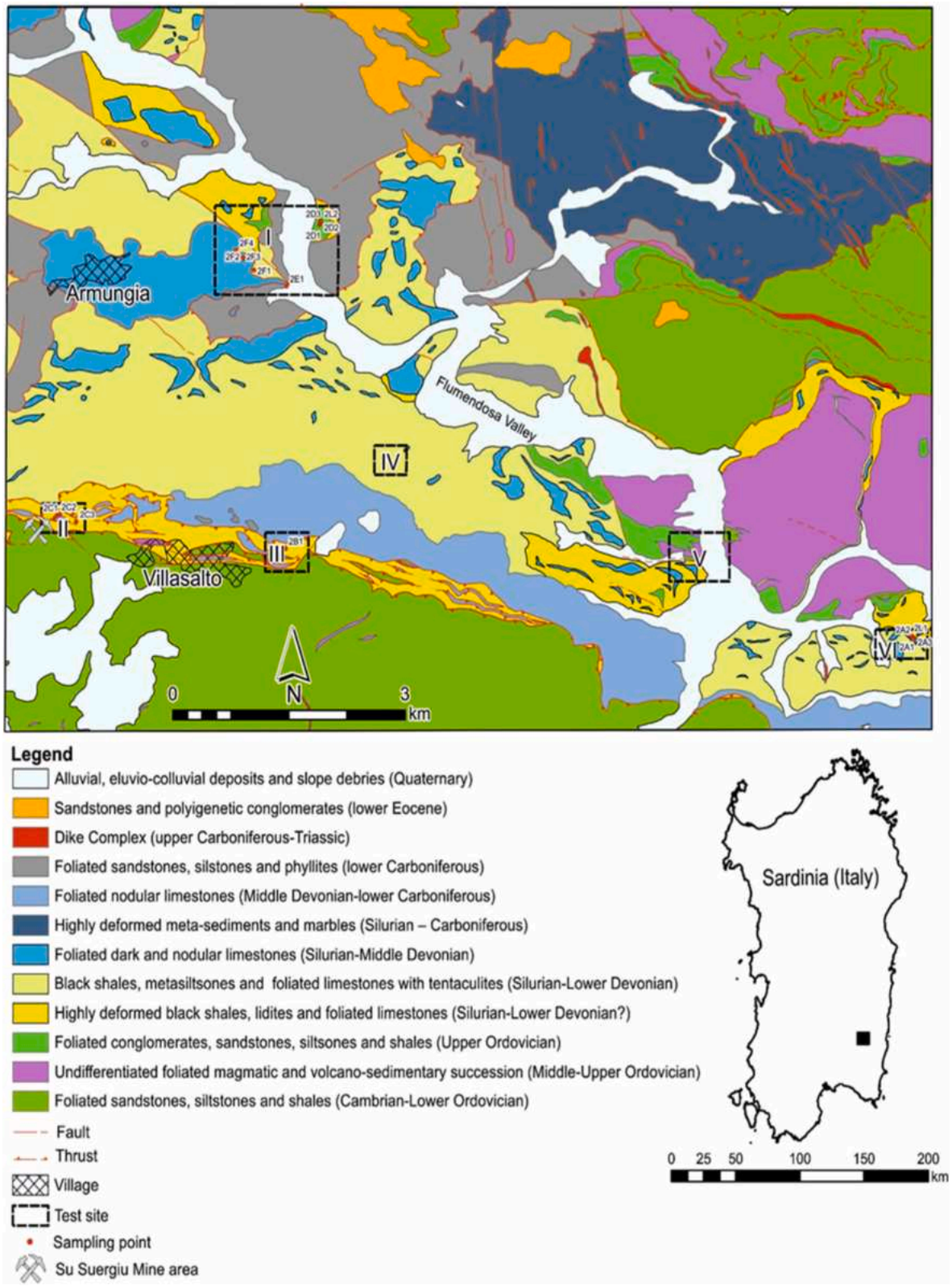

Fig. 1. *Study area and sampling points overlapping a simplified geological map of the Villasalto district* (Cidu et al., 2014; RAS, 2013).

the study area, U (ppm), Th (ppm) and K (%) contents were measured with an RS-230 BGO (Bismuth Germanate Oxide) Super–Spec portable radiation detector. A total number of 986 readings were taken at the six test sites represented in Fig. 1. The aim was to scan the black shale outcrops in the area of each test site. The radiometric data was processed and then graphically displayed on satellite maps.

2.2. Preparation and characterization of rock samples

Seventeen rock samples of about 2–3 kg each, were collected in

Fig. 2. Deformed black shale and quartz veins - Su Suergiu (Sardinia, Italy).

outcrops of the highly deformed Silurian black shale formation within the study area (special care was taken to avoid weathered rocks). The samples were packed into polyethene bags, tagged, and transported to the laboratory, where each specimen was manually crushed by using a mortar and pestle, homogenized (less than 1 mm grain size) and oven-dried for 12 h at 110 °C. Two sets of samples of about 100 gr were separated from the original samples. The samples were placed in 125 ml polycarbonate cylindrical containers (with a diameter of 9 cm and height of 2 cm). The first set was hermetically sealed and left undisturbed for a minimum of four weeks, in order to reach the radioactive equilibrium before carrying out the gamma-ray spectrometry. The other 17 samples from the second set were left open to enable the exhalation of radon from the surface during the test inside a sealed chamber. The apparent density (ρ_b) and the particle size distribution were determined for each sample (Table 1). To calculate the sample's apparent density, the mass measured by a balance in (gr) was divided by the volume of the sample. A container of known volume was fully filled with the soil sample to measure its volume.

2.3. Measurements of radionuclide activity concentration

The samples appropriately prepared as described in section 2.2 have been analyzed through a 1024-channel NaI (Tl) scintillation detector (3 × 3 inches) for the estimation of the radioactivity concentration of ^{226}Ra, ^{232}Th and ^{40}K. The acquisition of the spectra was carried out using the Ortec MAESTRO software. The specific gamma lines used to measure the radioactivity concentration of ^{226}Ra, ^{232}Th, and ^{40}K include 186 keV and 295 keV for ^{226}Ra, 238 keV and 2614 keV for ^{232}Th, and 1460 keV for ^{40}K. To separate the different gamma lines, the detector uses a process called energy discrimination. This involves setting a threshold energy level for the detector so that only gamma rays with energies above that level are counted. This allows the detector to distinguish between different gamma lines based on their energy levels. Energy calibration involves determining the relationship between gamma-ray energy and energy bins in a spectrum, while efficiency calibration involves determining the detection efficiency of the gamma spectroscopy system for a specific energy or range of energies using a standard reference source. The efficiency of gamma spectroscopy depends on several factors, including the type of detector, the energy of the gamma radiation, and the geometry of the sample being measured (Erdi-Krausz et al., 2003). We measured the efficiency of gamma spectroscopy by comparing the number of gamma rays detected by the detector to the number of gamma rays emitted by a known radioactive source (calibrated source of ^{137}Cs and ^{60}Co). The energy resolution was calculated to be 10.36%, concerning the full width of the peak at half of the maximum count level of 661 keV photopeak for the ^{137}Cs source. The IAEA uranium and thorium references (RGU1 and RGTh1) and high pure potassium nitrate (KNO_3) salt were employed to calibrate the spectrometer.

The spectrum of each analyzed sample was obtained as the weighted

Table 1
Particle size distribution of the tested samples.

Code*	ρ_b	Particle Size Distribution					
		0.5–1 mm	0.25–0.5 mm	0.125–0.25 mm	0.063–0.125 mm	0.038–0.063 mm	<0.038 mm
	g.cm^{-3}	% of retained					
#2A1	1.39	45.81	21.47	14.62	12.37	5.52	0.20
#2A2	1.36	49.91	21.18	13.53	10.35	4.38	0.65
#2A3	1.36	58.79	21.21	7.14	3.82	7.04	2.01
#2B1	1.30	55.19	14.38	11.55	10.27	7.24	1.37
#2C1	1.19	45.52	22.36	16.26	10.44	4.33	1.08
#2C2	1.32	51.55	20.44	13.06	8.97	4.79	1.20
#2C3	1.60	44.17	18.69	13.90	11.58	10.75	0.91
#2D1	1.43	52.45	20.47	9.73	5.92	8.71	2.71
#2D2	1.56	55.41	19.85	11.74	8.78	4.05	0.17
#2D3	1.43	54.57	19.12	11.57	9.98	4.57	0.19
#2E1	1.36	51.85	20.88	13.19	10.29	3.10	0.70
#2F1	1.34	49.26	19.33	12.78	13.38	5.05	0.20
#2F2	1.34	53.65	20.62	12.51	8.81	4.00	0.40
#2F3	1.28	5.58	23.72	43.74	24.66	2.19	0.10
#2F4	1.50	56.17	20.33	11.71	8.17	3.45	0.18
#2L1	1.37	70.78	14.86	7.03	3.01	3.82	0.50
#2L2	1.44	14.51	10.97	21.73	42.39	10.12	0.28

sum of the three spectra ^{238}U, ^{232}Th and ^{40}K, plus the background spectrum; the weight of each spectrum depends on the mass (i.e.: the activity) of the radioisotope in the sample under analysis. The specific activity of samples was estimated according to the maximum likelihood algorithm. The variance reduction technique was applied to calculate both the weights and the standard deviations. The correspondence between experimental data and theoretical values was verified by performing and graphing the linear combination of the three appropriately weighted spectra. The correspondence between calculated and experimental spectra was excellent in all cases; an example (*#2A2)* is given in Fig. 3. The ^{238}U, ^{232}Th and ^{40}K activity concentrations are estimated by applying the method above described, while the ^{226}Ra concentration is derived as an equivalent equilibrium concentration from the ^{238}U - ^{226}Ra mass ratio 1: 3.376×10^{-7} (Erdi-Krausz et al., 2003).

2.4. Estimation of Rn emanation coefficient and production rate

One of the most common techniques used to monitor the radon activity of a given material is the *enclosed sample method*, by which the real-time concentration of Rn gas is measured inside a sealed chamber that contains both the sample and the radon monitoring system (Leonardi et al., 2018). A pressure-resistant vacuum glass container of 6.2 l effective volume was used as an accumulation chamber (see Fig. 4) and a vacuum pump to maintain the system's airtightness. The radon activity concentration, the temperature and the relative humidity were simultaneously measured with a monitoring instrument Radex MR-107 (sampling time = 1 h; minimum time measurement = 72 h). The real-time activity concentration $C_{(t)}$ was acquired, graphed and elaborated afterwards. $C_{(t)}$ was modelled according to the two-dimensional diffusion theory expressed by Equation (1) (Sahoo and Mayya, 2010):

$$C_{(t)} = C_0 e^{-t\lambda_e} + C_m\left(1 - e^{-t\lambda_e}\right) \quad (1)$$

where λ_e is the effective radon decay constant (h^{-1}), which accounts for the radon decay, the leak rate and the *back diffusion*; C_0 and C_m are the radon activity concentrations ($Bq.m^{-3}$) respectively at $t = 0$ and $t = \infty$ (Leonardi et al., 2018).

The values of λ_e and C_m were extrapolated using the nonlinear least-squares fitting of the experimental data with Equation (1) (see Fig. 5) (Tan and Xiao, 2011; Kemmer and Keller, 2010). The *radon emanation coefficient* (E) was then calculated according to Equation (2) (Ishimori et al., 2013):

$$E = C_m V_{eff} / A_R W \quad (2)$$

Fig. 4. Experimental set-up for radon exhalation rate measurement (accumulation chamber, samples, and the Quarta-RAD software).

where W is the sample weight (kg) and A_R is the mass activity of ^{226}Ra in the sample ($Bq.kg^{-1}$) which was estimated based on uranium activity through the use of conversion factors or ratios between the two isotopes. It is important to note that V_{eff} refers to the effective volume of the radon chamber, which is a crucial factor in the calculation of radon concentration. V_{eff} takes into account the volume of the chamber as well as any air exchange that may occur during the measurement period. The *radon production rate* P_{Rn} ($Bq.m^{-3}.h^{-1}$) was also estimated according to Equation (3) (Ishimori et al., 2013; Pereira and Neves, 2012)

$$P_{Rn} = A_R E_b \lambda_e \quad (3)$$

where $\rangle_b$ is the estimated apparent density reported in Table 1.

3. Results

3.1. Radionuclide activity concentration

3.1.1. Field measurements

The results of the gamma-ray spectrometry performed in the six selected test sites in Fig. 1 are reported in Table 2. It is important to note that the use of different units for reporting radioactivity in field and laboratory samples is appropriate for the respective samples. When working in the field, we often deal with large rock masses where it may not be practical to determine the exact mass. Therefore, using units such

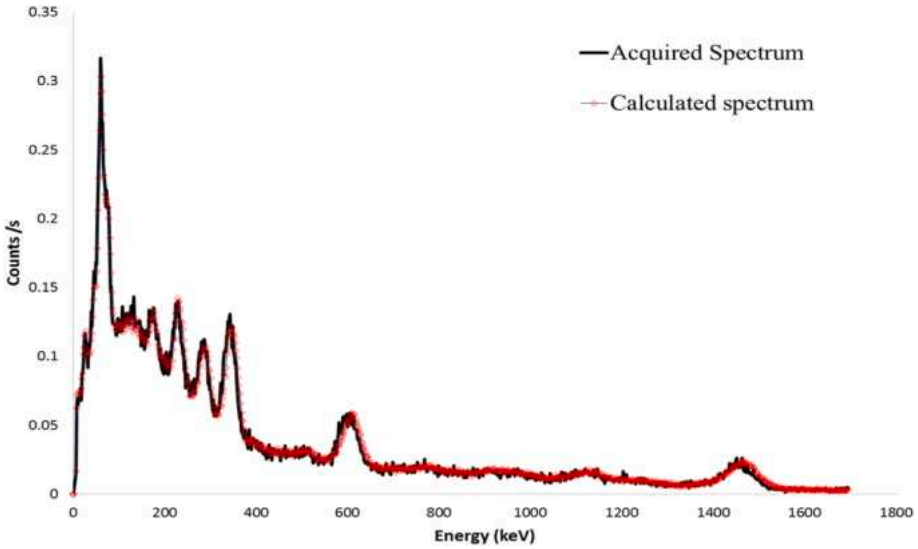

Fig. 3. Acquired spectrum and calculated spectrum (red) for sample #2A2.

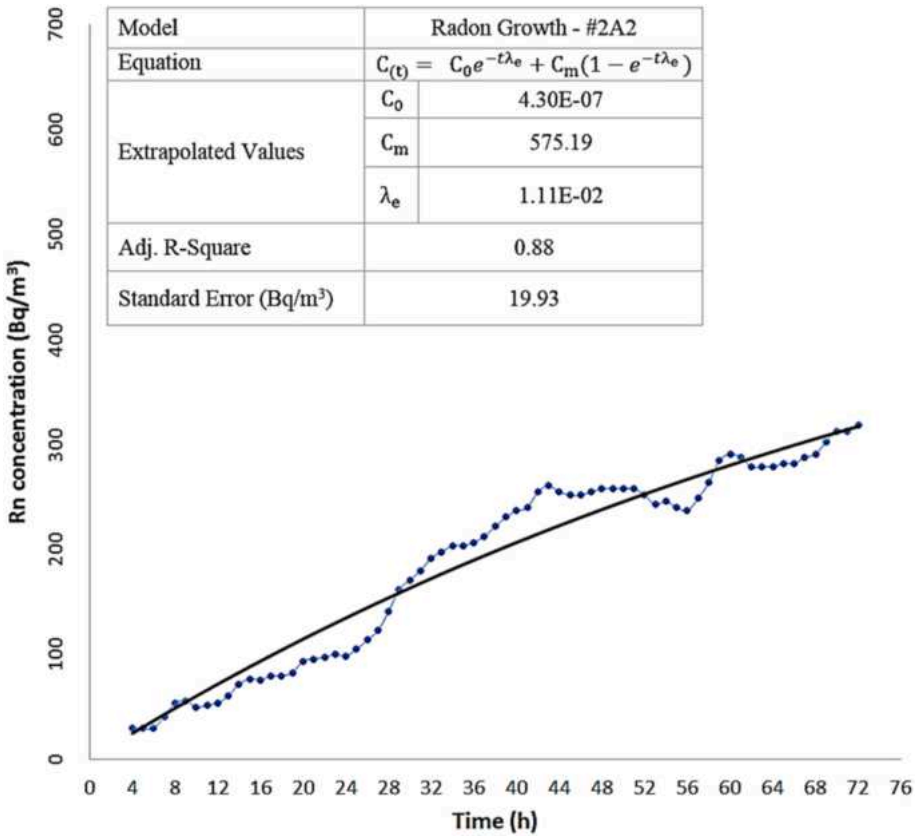

Fig. 5. Radon activity growth inside the sealed chamber and nonlinear least-squares fit of measured radon activity with Equation (1).

Table 2
Descriptive statistics for the distribution of natural radionuclides and attributed dose rates in the test sites.

Site Code	Number of readings	U (ppm)		Th (ppm)		K (%)		Dose Rate (nSv/h)	
		Mean ± SD	Range	Mean ± SD	Range	Mean ± SD	Range	Mean ± SD	Range
I	485	16.47 ± 12.72	[0.2–55.4]	11.91 ± 4.51	[2.7–27.7]	3.06 ± 1.03	[0.6–6.7]	195.56 ± 93.05	[32.7–483.7]
II	125	8.32 ± 3.3	[3.1–17.1]	9.82 ± 2.11	[4.1–15.3]	2.24 ± 0.59	[1.3–3.6]	122.26 ± 31.99	[68.9–191.4]
III	31	7.90 ± 3.16	[4.1–14.1]	11.80 ± 2.58	[8.4–16.8]	2.85 ± 0.37	[1.8–3.4]	135.49 ± 16.83	[110.0–165.1]
IV	18	4.24 ± 1.68	[2.3–9.3]	15.76 ± 3.14	[6.3–20.2]	3.3 ± 0.27	[2.5–3.6]	131.50 ± 11.72	[109.4–155.1]
V	120	6.35 ± 2.77	[1.8–15.5]	11.60 ± 3.68	[3.7–20.8]	3.93 ± 1.73	[1.5–8.1]	141.93 ± 36.67	[74.2–218.1]
VI	207	12.85 ± 6.20	[2.9–27.9]	11.98 ± 2.33	[6.0–18.1]	2.72 ± 0.5	[1.7–4.1]	164.05 ± 40.13	[77.6–260.4]
Total	986	12.96 ± 10.33	[0.2–55.4]	11.52 ± 3.84	[2.7–27.7]	2.98 ± 1.10	[0.6–8.1]	169.97 ± 75.58	[32.7–483.7]

as parts per million (ppm) and percentage (%), which are relative measurements, is more practical. However, in the laboratory, we can measure the exact mass of the samples, making units such as becquerels per kilogram (bk.kg^{-1}) more appropriate. We have provided the conversion factor (1 ppm corresponds to 12.35 Bq.kg^{-1} for ^{238}U and 4.06 Bq.kg^{-1} for ^{232}Th; 1% of ^{40}K is 313 Bq.kg^{-1}) (Erdi-Krausz et al., 2003)for those who wish to compare the two measurement systems. Although we have utilized different units for reporting radioactivity in field and laboratory samples, we have attempted to establish consistency between the two measuring systems by providing conversion factors, where necessary.

Fig. 6 shows the map of the uranium concentration in the test sites. The maximum recorded value of uranium activity concentration is 55.4 ppm (684.19 Bq.kg^{-1}). Figs. 7 and 8 show the corresponding maps for thorium and potassium.

The histograms of the radionuclide's activity concentration are reported in Fig. 9. It's worth highlighting as most of the readings for uranium are in the range of 6–30 ppm (74.1–370 Bq.kg^{-1}), a relatively high level if compared to the world average of 2.8 ppm (UNSCEAR, 2008), which confirms the uranium enrichment in the area under consideration. The peaks of the thorium concentrations represent the most common values between 6 and 12 ppm which is the same range as the worldwide averages (7.2 ppm (UNSCEAR, 2008),). The peak of potassium data spread is from about 2.2 % to 2.8 %. which is relatively two times the worldwide average for the elemental concentration of 40K in soil (1.3% (UNSCEAR, 2008),)

3.1.2. *Laboratory measurements*

The results of the laboratory tests performed on the 17 samples of Silurian black shales are reported in Table 3. The activity concentration of the terrestrial radionuclides was found between 103.32 and 384.51 Bq.kg^{-1} for ^{226}Ra, between 23.84 and 63.62 Bq.kg^{-1} for ^{232}Th and between 216.70 and 1450.13 Bq.kg^{-1} for ^{40}K, with mean values of 256.32 ± 87, 44.16 ± 9.47 and 856.28 ± 392.41, respectively.

According to test results, the mean activity concentration of ^{232}Th (11.52 ± 3.84 ppm or 46.77 ± 15.59 Bq.kg^{-1}) and ^{40}K (2.98 ± 1.1 % or 932.74 ± 344.3 Bq.kg^{-1}) measured in-situ (Table 2) are in accordance with the values obtained through laboratory gamma-ray spectrometry (Table 3). Except for ^{232}Th, the calculated mean values were found significantly higher than the worldwide average activity reported by

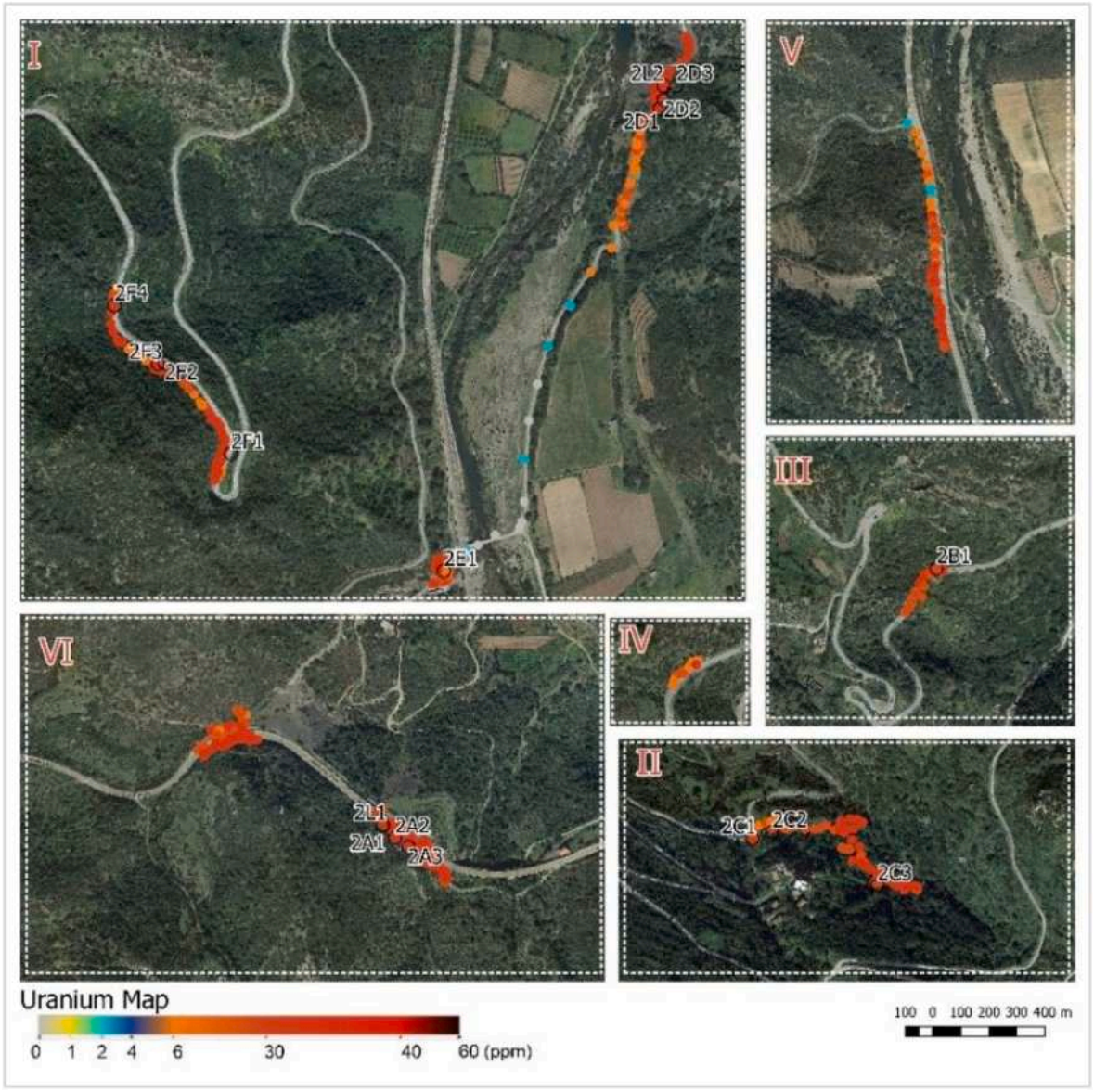

Fig. 6. Activity concentration of U (ppm) at the test sites (see also Fig. 1).

(UNSCEAR, 2008): 32 Bq.kg^{-1} (^{226}Ra), 45 Bq.kg^{-1} (^{232}Th) and 412 Bq.kg^{-1} (^{40}K). However, it should be noted that the measured values of radionuclide concentrations are consistent with those reported for black shales in other parts of the world (Ketris and Yudovich, 2009). The elevated concentration of uranium and low activity of thorium in the tested samples can be explained by the behaviour of these radioisotopes in the environment. The Th/U ratio indicates the relative depletion or enrichment of radioisotopes. The expected Th/U ratio for the normal continental crust is about 4. Alteration, weathering, or other metasomatic activities can change this ratio (Örgün et al., 2005). As shown in Fig. 9, Th/U values are much lower than 4; moreover, the weak correlation between uranium and thorium in black shale samples (Fig. 10) could be due to various geological processes. For example, the presence of other minerals or elements in the sample can affect the concentration of uranium and thorium. Additionally, weathering can alter the distribution of these elements within the sample. However, the good correlation coefficient between the Th/U and U charts (Fig. 11) suggests that the ratio of thorium to uranium remains consistent across the samples and this can provide insight into the geological history of the area. By studying this ratio, geologists can better understand the formation and evolution of the Silurian black shale deposits of the Villasalto region.

Uranium enrichment is likely to have occurred in organic matter-rich sediments during a low-rate sedimentary deposition, testified by the occurrence of condensed levels containing authigenic minerals (i.e., phosphates). The rising base levels during the post-glacial transgression phases likely thwarted the river supply, causing sediment starvation. Terrigenous inputs were very low and thin deposits represent a period larger than 10^5–10^7 years. The mechanism that transfers U from the water to the organic deposit is not diluted by sediments and consequently increases the concentration in the deposit. However, other processes like remobilization and re-concentration of uranium during metamorphic alterations, as well as during the mesothermal mineralization phases, might have taken place. The redox environment, pH, U oxidation state (U(IV), U(VI)) and the abundance of CO_3 are the principal determinants for U mobility (Cumberland et al., 2021). Weathering and alteration processes can also lead to an increase of ^{226} Ra concentration. Considering the relative solubility over long periods, ^{226}Ra has a greater chance of being transported from the host rocks and being redeposited (Perry and I Marcellus Shale Team, 2011; East, 2014; Thu et al., 2019). Unlike ^{226}Ra, ^{232}Th is very stable, it does not dissolve in a

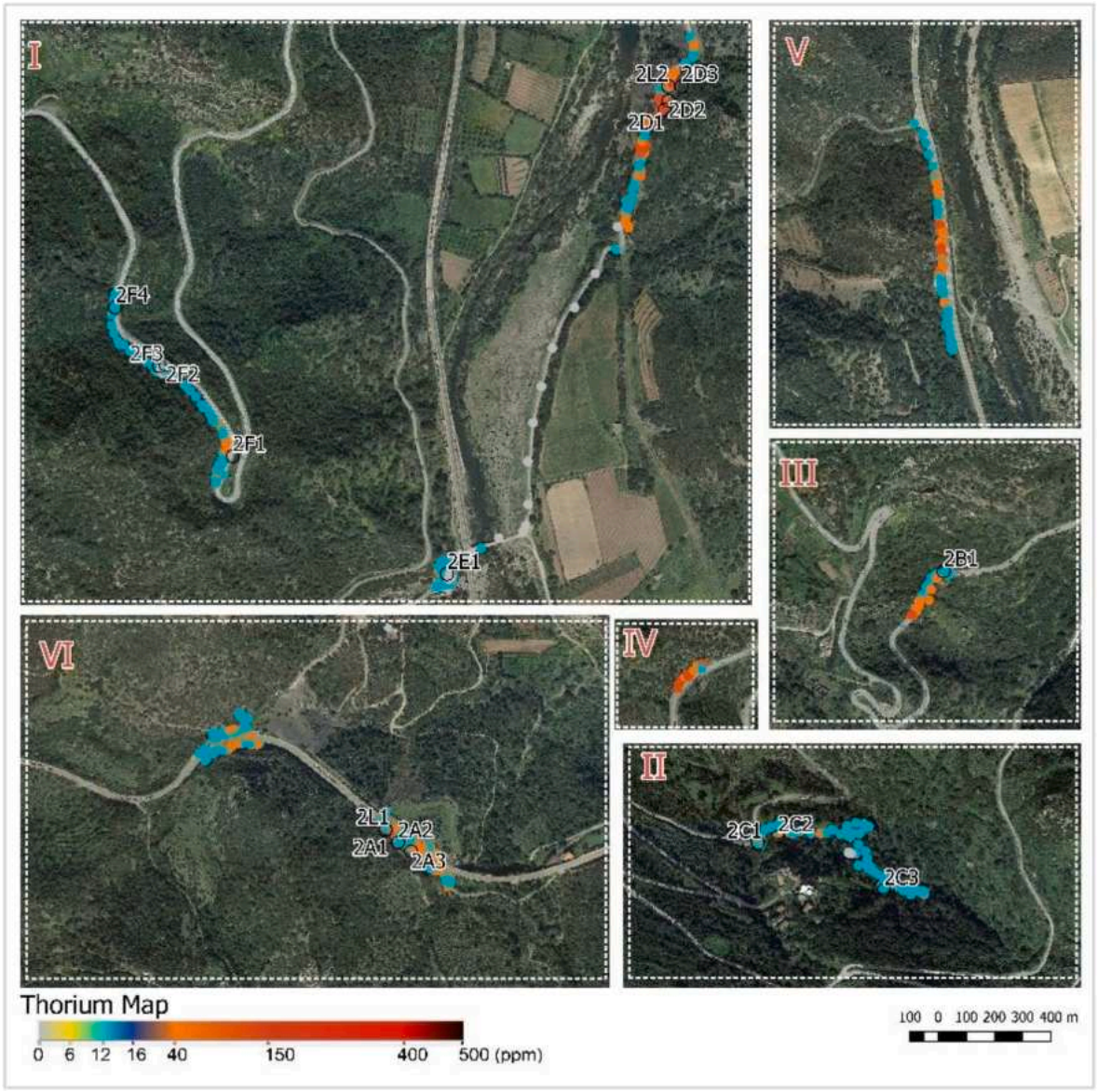

Fig. 7. Activity concentration of Th (ppm) at the test sites (see also Fig. 1).

solution and cannot be transported by water during weathering processes (Schön, 2015). This may be the reason behind the relatively high ^{226}Ra concentration and low ^{232}Th contents recorded for most of the tested samples. The ^{232}Th content is probably related to the terrigenous phases, like clay minerals or other phyllosilicates.

The radionuclide activity levels obtained in this research are similar to the results of a previous study on uranium, thorium and potassium carried out for the black Shales of the Bazhenov formation located in the west Siberian marine basin (Zanin et al., 2016).

3.2. Radiation hazard indexes

Once the activity concentration of terrestrial radionuclides (^{226}Ra, ^{232}Th, and ^{40}K) is determined, it is possible to estimate the radiological indexes to be used in the assessment of public exposure to natural radiation. The most commonly used radiation hazard indexes are the radium equivalent activity Ra_{eq} (Bq.kg^{-1}), the outdoor gamma-ray dose rate D (nGy.h^{-1}) and the annual effective dose AED (mSv.y^{-1}).

The above-mentioned indexes can be calculated according to Equations (4)–(6) (UNSCEAR, 2008) respectively:

$$Ra_{eq}\left(\frac{Bq}{Kg}\right) = C_{Ra} + 1.43\ C_{Th} + 0.077\ C_K \tag{4}$$

$$D\left(\frac{nGy}{h}\right) = 0.462\ C_{Ra} + 0.462\ C_{Th} + 0.0417\ C_K \tag{5}$$

$$AED\left(\frac{mSv}{y}\right) = \mathrm{D} \times O_f \times 8760 \times 0.7 \times 10^{-6} \tag{6}$$

where C_{Ra}, C_{Th}, and C_K are respectively the activity concentrations of radionuclides ^{226}Ra, ^{232}Th and ^{40}K (Bq.kg^{-1}) and O_f is the occupation factor, which is the fraction of the year hypothetically spent outdoors (UNSCEAR, 2008) (the suggested value is 0.2). Table 4 reports the values of the radiation hazard indexes, which have been calculated based on the laboratory and in-situ gamma-ray spectrometry results. The Ra_{eq} mean values were found below the reference level of 370 Bq.kg^{-1} (Beretka and Mathew, 1985), which corresponds to an external effective dose of 1.5 mGy (1 mSv.y^{-1}). The mean values of the calculated gamma-ray dose rate are about 3 times the reported population-weighted mean value of 58 nGy.h^{-1} for a regular area

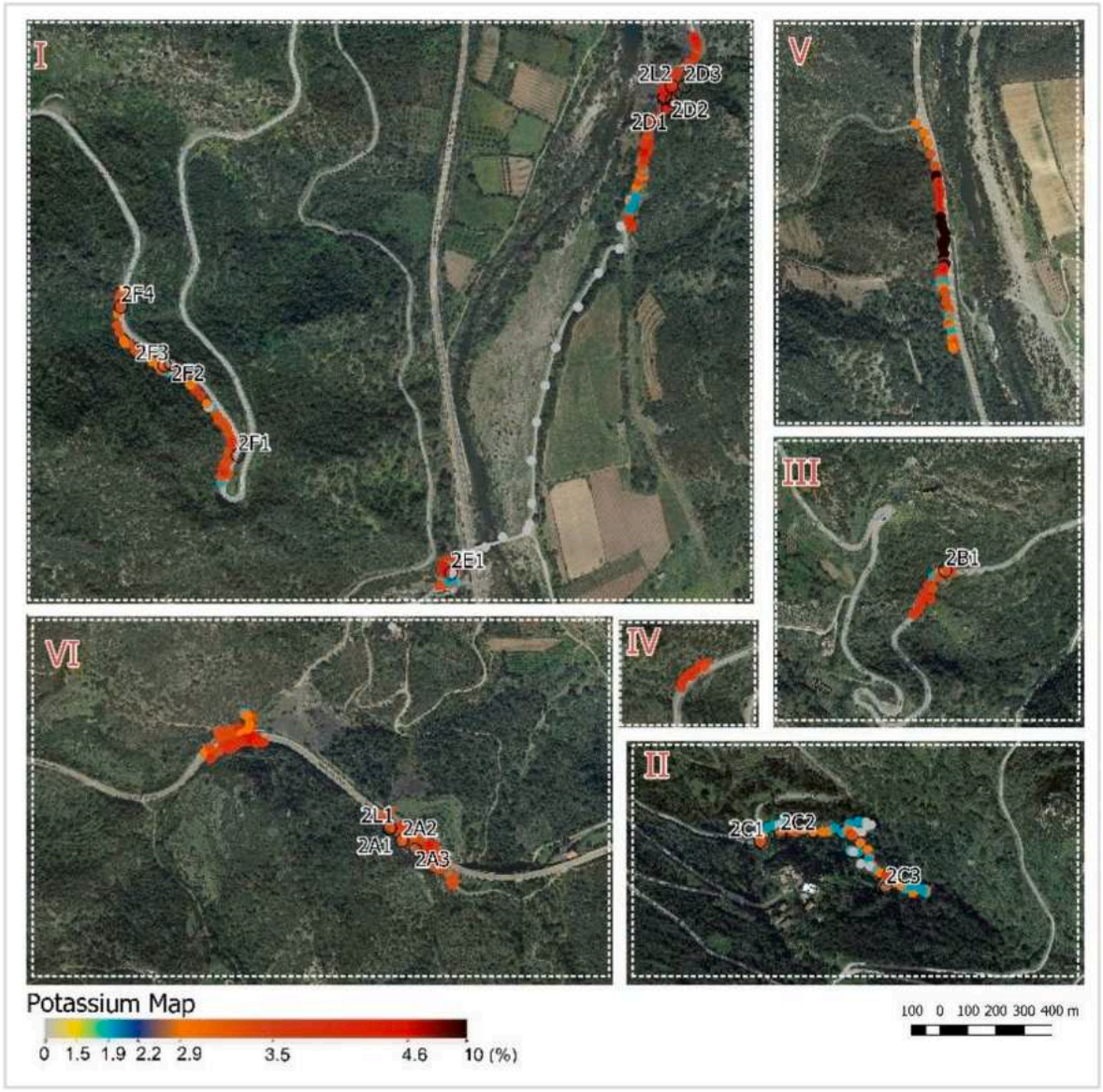

Fig. 8. Activity concentration of K (%) at the test sites (see also Fig. 1).

(UNSCEAR, 2008). The mean annual effective dose values are within the worldwide ranges (0.01–0.43 mSv.y^{-1}) (UNSCEAR, 2008).

3.3. Emanation and exhalation of radon

The release of gas radon to the air is governed by three main processes: the emanation of radon from radium-bearing grains, the accumulation of radon atoms in pore spaces, the transport of radon from porous media to the surface and the subsequent exhalation from the soil surface to the atmosphere (Ishimori et al., 2013). The emanation of radon depends on the ^{226}Ra distribution within the rock, the rock's particle size, its moisture content and mineralogy (Ishimori et al., 2013). Table 5 shows the estimated values of radon activity concentration C_m (Bq.m^{-3}). Using the extrapolated values of C_m and the effective decay constant (λ_e), the radon emanation coefficient (E) and the radon production rate (P_{Rn}) were calculated. The highest and lowest values of P_{Rn} are 212.54 and 524.27 Bq.m^{-3}.h^{-1} respectively; while the mean value is about 348 Bq.m^{-3}.h^{-1}. Fig. 12 shows the distribution of the calculated radon production rates.

Mean values of P_{Rn} in the range 88–382 Bq.m^{-3}.h^{-1} were reported in a recent study (Pereira and Neves, 2012) for two sets of borehole samples collected from the Hercynian granites of the northern and central parts of Portugal. Furthermore, the radon production rate of three surface samples collected from the same unit, but with different degrees of alteration, was found to be 403, 598 and 653 Bq.m^{-3}.h^{-1} (considering an increasing order for the degree of alteration). A simple comparison between the values of radon production rates reported by (Pereira and Neves, 2012) and the estimated radon production rates in this study reveals that the radon production rate of black shales, especially those with higher alteration degrees, is similar to the rates found for granite formations, which are generally believed to have enhanced geogenic radon potential.

3.4. Investigation of correlations

In order to explore the relationships between E, the steady-state activity concentration of radon (C_m) and the contents of radium, thorium and potassium (see Tables 3 and 5), a Pearson correlation matrix was built (Table 6). A significant positive correlation was found between C_m and E (0.74). A relatively good correlation was found between C_m and the radium content (0.65). (Thu et al., 2019) reported that radon emanation is not dependent on the radium content of the soil

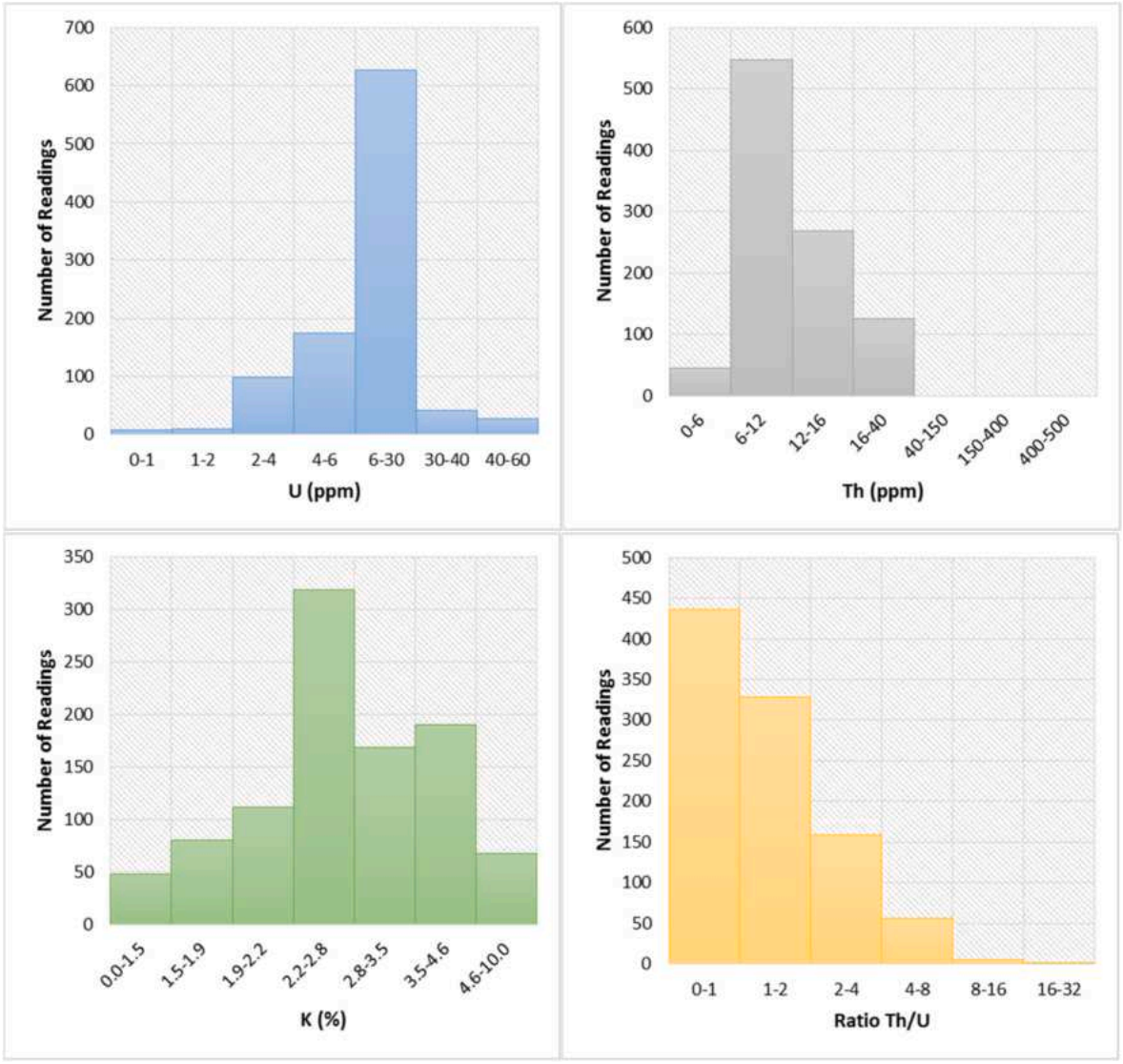

Fig. 9. Histograms of measured radionuclide concentrations at the test sites and Th/U ratios.

Table 3
Statistics for radionuclide concentration of the tested samples.

Code	Radionuclide Concentration (Bq.kg^{-1})			D (nGyh)
	$A_{Ra} \pm \sigma$*	$A_{Th} \pm \sigma$	$A_K \pm \sigma$	
#2A1	258.36 ± 3.22	41.17 ± 2.48	487.93 ± 90.12	164.57
#2A2	286.70 ± 3.60	53.67 ± 2.76	820.20 ± 100.67	199.08
#2A3	313.98 ± 3.86	39.68 ± 2.96	534.65 ± 107.95	191.32
#2B1	200.78 ± 3.46	44.41 ± 2.66	1188.57 ± 96.91	169.15
#2C1	103.32 ± 2.85	47.83 ± 2.19	1292.58 ± 79.63	130.52
#2C2	136.56 ± 2.77	56.57 ± 2.13	1148.48 ± 77.58	145.15
#2C3	151.73 ± 2.80	37.39 ± 2.15	846.71 ± 78.46	127.99
#2D1	238.81 ± 3.47	63.62 ± 2.66	1420.12 ± 96.97	207.98
#2D2	162.44 ± 2.77	46.03 ± 2.13	1394.35 ± 77.64	160.99
#2D3	290.98 ± 3.36	43.18 ± 2.58	965.75 ± 93.97	200.79
#2E1	277.33 ± 4.19	49.27 ± 3.22	1450.13 ± 117.24	218.36
#2F1	331.24 ± 4.87	34.50 ± 3.74	490.52 ± 136.23	194.33
#2F2	384.51 ± 4.33	32.63 ± 3.33	516.92 ± 121.10	218.91
#2F3	382.36 ± 5.29	50.61 ± 4.07	623.91 ± 148.13	233.23
#2F4	180.48 ± 2.53	23.84 ± 1.94	578.35 ± 70.75	121.89
#2L1	321.75 ± 3.86	40.87 ± 2.97	580.97 ± 108.02	197.56
#2L2	336.08 ± 3.92	45.52 ± 3.02	216.70 ± 109.82	191.80

σ*: Associated Uncertainty (1σ).

sample. A previous study (East, 2014) revealed that the radium adsorbs onto oxidized Fe phases, which makes radium more concentrated on the surface of the soil grains. However, black shales are formed in low-oxygen environments and therefore the concentration of radium on the grain surfaces does not often occur. This fact may explain the reason for the lack of correlation (0.02) between ^{226}Ra and the radon emanation coefficient (see Table 6).

The correlation coefficients obtained for the emanation coefficient, the radon activity concentration and the radium concentration are similar to values reported by (Thu et al., 2019). Moreover, a medium positive correlation was found between ^{40}K and ^{232}Th contents, however, the correlation coefficient of ^{226}Ra vs. ^{232}Th and ^{226}Ra vs. ^{40}K was found to be −0.13 and −0.61, respectively. The significant inverse correlation found between uranium and potassium (−0.61) is comparable to the findings of another study (Zanin et al., 2016), which indicates a correlation of −0.62 (Zanin et al., 2016).) reported a significant positive correlation (0.91) between U concentration in black shales and organic carbon, and also a negative correlation (−0.52) between K and organic carbon. In other words, in that research, they indirectly reported an inverse correlation between uranium and potassium which is in agreement with the findings of our research. The content of small particles in a rock/soil sample (i.e. silty-clay size) can make a difference in the resulting radon emanation coefficient (Thu et al., 2019; Zanin et al.,

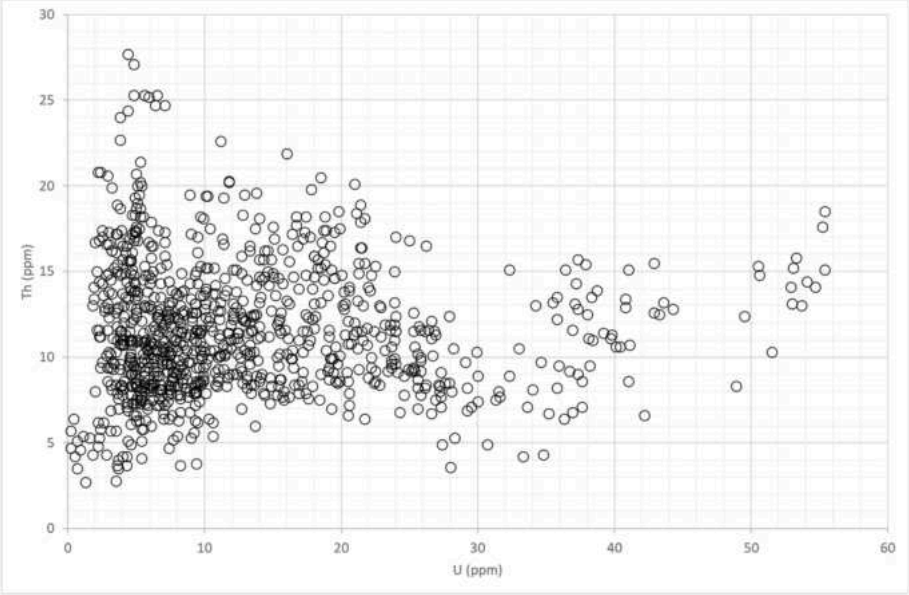

Fig. 10. Correlation charts between Th and U.

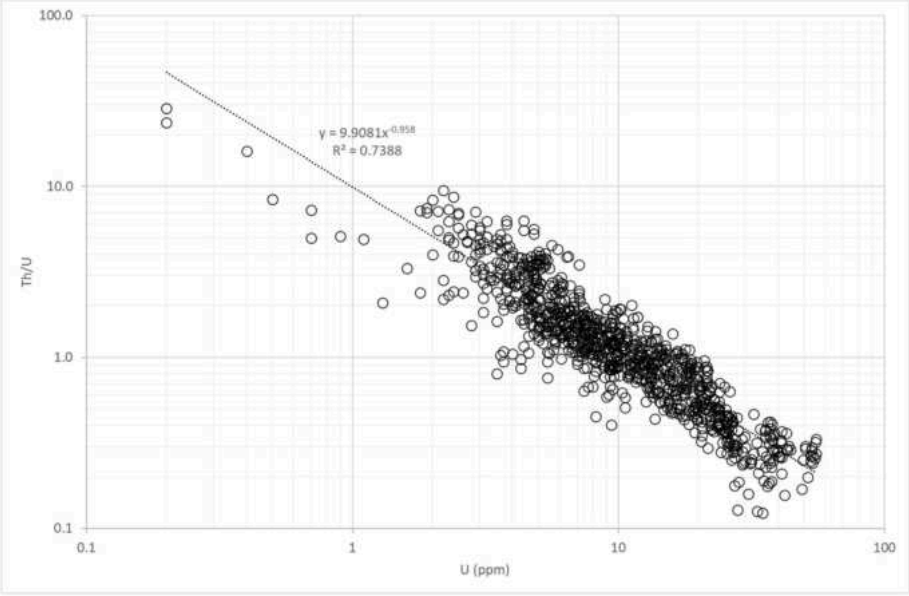

Fig. 11. Correlation charts between Th/U and U in ppm.

Table 4
Values of the radiation hazard indexes calculated based on the results of laboratory and in-situ gamma-ray spectrometry.

	Ra_{eq} ($Bq.kg^{-1}$)		D ($nSv.h^{-1}$)		AED ($mSv.y^{-1}$)	
	Mean ± SD	Range	Mean ± SD	Range	Mean ± SD	Range
Laboratory test	327.22 ± 87.74	177.85–466.13	180.80 ± 34.12	121.89–233.23	0.22 ± 0.04	0.15–0.29
Field test	299.07 ± 138.62	53.86–883.18	169.97 ± 75.58	32.70–483.70	0.21 ± 0.09	0.04–0.59

2016). Therefore, the correlation between E (Table 5) and the particle size intervals (Table 1) of the tested samples has been evaluated using Pearson's correlation matrix (Table 7). A reasonably good correlation (0.77) was found between the radon emanation coefficient and soil content with a size less than 0.038 mm (i.e., silt and clay). This is also consistent with the results of the study done by (Thu et al., 2019).

4. Discussion

Various methods proposed by the international literature can be used to produce a GRP map. In some cases, radon values of regions with sufficient data have been extended to areas with alleged similar geology or geogenic maps of European territories that have been produced based on geological units, mainly defined based on lithology and age (Bossew

Table 5
Statistics for radon characteristics of the tested samples.

Code	$C_m \pm SE^*$ (Bq.m^{-3})	E	P_{Rn} (Bq.m^{-3}.h^{-1})
#2A1	553.36 ± 16.33	0.13	273.12
#2A2	575.19 ± 19.93	0.12	524.27
#2A3	946.31 ± 34.65	0.18	467.05
#2B1	262.45 ± 16.58	0.08	381.21
#2C1	215.10 ± 25.06	0.14	312.43
#2C2	239.21 ± 35.35	0.11	345.86
#2C3	307.51 ± 30.30	0.10	446.67
#2D1	874.33 ± 23.05	0.21	431.53
#2D2	266.18 ± 23.25	0.09	389.23
#2D3	284.25 ± 20.49	0.06	412.88
#2E1	621.31 ± 30.64	0.14	306.65
#2F1	444.66 ± 27.16	0.08	219.47
#2F2	822.13 ± 34.92	0.13	238.83
#2F3	430.64 ± 10.55	0.07	212.54
#2F4	204.62 ± 11.36	0.06	298.20
#2L1	595.25 ± 30.05	0.11	293.79
#2L2	717.64 ± 22.37	0.12	354.19

SE: Standard Error of the Estimated Value, σ*: Associated Uncertainty (1σ).*

et al., 2020). The problem with 'extrapolating radon-related parameters to similar geologies' is the large variability of the radon potential within the same geological unit, which makes that methodology sometimes ambiguous. The geological conditions that control the enrichment of U (and subsequently radon) in lithotypes are complex and the lithology cannot always represent the real occurrence of U enrichment. In general, lithotypes are classified with textural and compositional criteria. The latter criterion is based on the main and most common minerals in the crust. Therefore, rocks classified as the same category from a lithological point of view may have different compositions of accessory phases, which may have very different U contents. Rocks can hold U enrichments according to geodynamic, stratigraphic, environmental and geochemical features, climatic conditions and, mainly for sedimentary rocks, the composition of the source areas that feed the sedimentary basins. Thus, it can be assumed that different geological evolutions related to the palaeogeography of the geological regions do not allow to automatic export of the measurements performed in other geological regions, in the absence of appropriate measurements that define the contents of radon-producing elements.

In contrast, the Silurian black shales are ampelitic deposits that, due to the global geological conditions prevailing during their deposition, related to the Great Glacial Crisis of the late Ordovician, produced similar geochemical oceanic conditions of global dimensions. These conditions provided characteristic clay-carbon deposits with high uranium concentrations over large areas. The broad uniformity of Silurian black shale compositions allows when present, uranium values to be used predictively, even in the absence of local measurements, to produce a GRP map. In highly deformed areas, such as Sardinia, Silurian black schists are almost always involved in cataclastic zones associated with thrust due to their mechanical characteristics. Depending on the intensity of deformation, cataclastic zones may consist of several stratigraphic levels and different lithotypes, which complicates the interpretation and predictive use for GRP maps. In addition, cataclastic belts may be the site of fluid circulations that mobilise elements and change the original compositions of lithotypes. As a matter of fact, a geogenic potential map must be preliminary drawn to take into account the local geological condition and the geodynamic environment from which they derive.

5. Conclusions

Silurian black shales are clay deposits that have distinctive compositional characteristics related to the stratigraphic conditions of strong

Table 6
Correlation matrix between radon concentration, emanation coefficient and radionuclide concentrations of the tested samples.

Variables	C(m)	E	^{226}Ra	^{232}Th	^{40}K
Cm (Bq/m^3)	1.00				
E	**0.74**	1.00			
^{226}Ra (Bq.kg^{-1})	**0.65**	**0.02**	1.00		
^{232}Th (Bq.kg^{-1})	–	–	**−0.13**	1.00	
^{40}K (Bq.kg^{-1})	–	–	**−0.61**	**0.57**	1.00

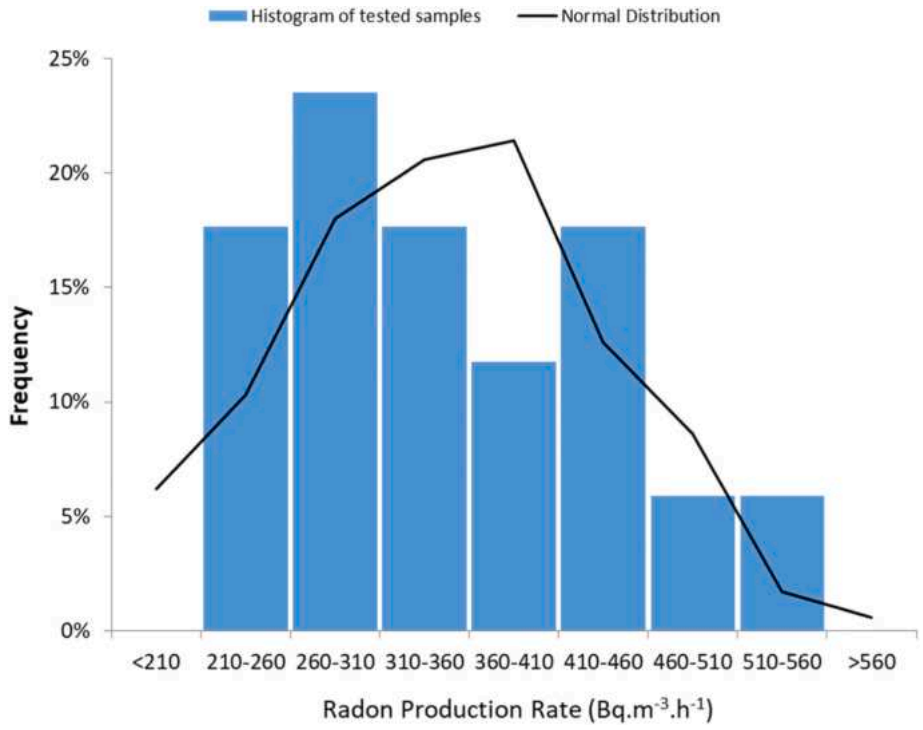

Fig. 12. Distribution of the radon production rates (Bq.m^{-3}.h^{-1}) obtained from the analysis of 17 black shale samples.

Table 7
Pearson's correlation matrix between radon emanation coefficient and particle size distribution.

Variables		e	Particle Size (mm)					
			[0.5–1]	[0.25–0.5]	[0.125–0.25]	[0.063–0.125]	[0.038–0.063]	[<0.038]
e		1.00						
Particle Size (mm)	*[0.5 - 1]*	**0.14**	1.00					
	[0.25 - 0.5]	**0.14**	0.00	1.00				
	[0.125-0.25]	**−0.29**	−0.91	0.22	1.00			
	[0.063-0.125]	**−0.19**	−0.87	−0.42	0.65	1.00		
	[0.038 - 0.063]	**0.36**	−0.14	−0.52	−0.20	0.29	1.00	
	[<0.038]	**0.77**	0.27	0.07	−0.36	−0.37	0.46	1.00

anoxicity in the sedimentary basin, resulting from the geological and glacioeustatic conditions they experienced. Strong compositional anomalies, for example in organic matter and many other chemical elements, including uranium, make them compositionally significant clay deposits. A large number of studies on black shales and the environmental aspects of their formation have been conducted over the past decades. In fact, among scientists, black shales are recognised as potential radon sources.

This study investigates in detail the natural radioactivity levels and the radon production rates of the highly deformed cataclastic zones largely produced by Silurian black shales of the Villasalto district. High concentrations of uranium and subsequently high radon exhalation rates were estimated. The results obtained in our study are similar to those reported in previous research carried out in Scandinavian and Eastern Europe. Using the estimated radionuclide concentrations, the radiation hazard indexes were also calculated for the study area under consideration. Even though the mean values were found below the reference levels, in some cases the hazard indexes exceeded the allowable limits. A considerably high radon production rate was estimated for the samples under investigation. Moreover, the correlation between the effective variables and the radon emanation coefficient was investigated. A high positive correlation was found between the radon emanation coefficient (E) and the radon activity concentration (Cm). The very fine texture and the rock's propensity for fissility appear to be an effective variable in controlling radon emanation and production rate (PRn).

The results obtained can be used for radioprotection purposes and also as a valuable tool to identify the Radon Priority Areas in Sardinia. Furthermore, considering that geology is known as the main contributor to geogenic radon potential, the results found in our study can be used in order to predict the radon potential for the areas that are located in the same geology (Silurian black shales).

Declaration of competing interest

The authors declare that they have no conflict of interest to declare.

Data availability

No data was used for the research described in the article.

Acknowledgements

This research was part of a PhD thesis for the University of Cagliari, Italy. This work is part of the research projects funded by Fondazione di Sardegna and Regional Sardinian Government: RE-MINE-REstoration and remediation of abandoned MINE sites, [grant number F72F16003160002] and "Sustainable land management: the tools of geology for the environment" [grant number F75F21001270007].

References

Abumurad, K.M., Al-Tamimi, M., 2001. Emanation power of radon and its concentration in soil and rocks. Radiat. Meas. 34 (1–6), 423–426. https://doi.org/10.1016/S1350-4487(01)00199-8.

Aghdam, M., Mirsina, 2021. Modelling of Geogenic Radon in Sardinia and Health Risk Assessment." Università degli Studi di Cagliari. https://iris.unica.it/handle/11584/313168.

Aghdam, Mousavi, Mirsina, 2023. Technical Report Evaluation and Study of Radon Occupational Exposure Levels in Dams: A Case Study of the Gallery of Medau Zirimilis Dam (Sardinia, Italy). Journal of the European Radon Association.

Aghdam, M.M., DaPelo, S., Dentoni, V., Fanti, V., Bernardini, A., Randaccio, P., Chiriu, D., 2019. Measurements of indoor radon levels and gamma dose rates. In: Proceedings of the World Congress on New Technologies, vol. 0. https://doi.org/10.11159/icepr19.149.

Aghdam, Mousavi, Mirsina, Crowley, Quentin, Rocha, Carlos, Dentoni, Valentina, DaPelo, Stefania, Long, Stephanie, Savatier, Maxime, 2021. A study of natural radioactivity levels and radon/thoron release potential of bedrock and soil in southeastern Ireland. Int. J. Environ. Res. Publ. Health 18 (5), 2709. https://doi.org/10.3390/ijerph18052709.

Aghdam, Mousavi, Mirsina, Dentoni, Valentina, Da Pelo, Stefania, Crowley, Quentin, 2022. Detailed geogenic radon potential mapping using geospatial analysis of multiple geo-variables—a case study from a high-risk area in SE Ireland. Int. J. Environ. Res. Publ. Health 19 (23), 15910. https://doi.org/10.3390/IJERPH192315910.

Aghdam, Mousavi, Mirsina, Saad, Noha, Azab, Marc, Sadrnejad, Seyed Amirodin, 2023. Deformability of single layer diamatic space frame domes under non-symmetrical snow load and earthquake shaking. Results in Engineering, 100884. https://doi.org/10.1016/j.rineng.2023.100884.

aldin Sadrnejad, Amir, Nikkhah, Majid, Mousavi Aghdam, Mirsina, Zahra Sharif Tehrani, 2017. Internal Damage Assessment of Concrete Arch Dam by Multi-Laminate Model upon Recorded Micro-geodesy Data.

Algeo, T.J., Tribovillard, N., 2009. Environmental Analysis of Paleoceanographic Systems Based on Molybdenum – Uranium Covariation" 268: 211–25. https://doi.org/10.1016/j.chemgeo.2009.09.001.

Appleton, J.D., Miles, J.C.H., 2010. A statistical evaluation of the geogenic controls on indoor radon concentrations and radon risk. J. Environ. Radioact. 101 (10), 799–803. https://doi.org/10.1016/j.jenvrad.2009.06.002.

Appleton, J.D., Miles, J.C.H., Green, B.M.R., Larmour, R., 2008. Pilot study of the application of tellus airborne radiometric and soil geochemical data for radon mapping. J. Environ. Radioact. 99 (10), 1687–1697. https://doi.org/10.1016/j.jenvrad.2008.03.011.

Awan, Tariq Ahmed, Arshid, Muhammad Usman, Sarmad Riaz, Malik, Houda, Moustafa, Abdallah, Mirvat, Shahkar, Muhammad, Mousavi Aghdam, Mirsina, Azab, Marc, 2022. Sub-surface geotechnical data visualization of inaccessible sites using {GIS}. ISPRS Int. J. Geo-Inf. 11 (7), 368. https://doi.org/10.3390/ijgi11070368.

Barca, S., Melis, E., Annino, E., Cincotti, F., Ulzega, A., Orrù, P., Pintus, C., 2005. Note Illustrative Della Carta Geologica d'Italia Alla Scala 1: 50.000, Foglio 557, Cagliari. Servizio Geologico d'Italia.

Baskaran, Mark, 2016. Radon: a tracer for geological, geophysical and geochemical studies. In: Radon: A Tracer for Geological, Geophysical and Geochemical Studies. Springer International Publishing. https://doi.org/10.1007/978-3-319-21329-3.

Baucon, Andrea, Corradini, Carlo, Floris, Matteo, Briguglio, Antonino, Cabella, Roberto, Campomenosi, Nicola, Piazza, Michele, Corriga, Maria G., 2020. Life in near-anoxic conditions: a case study of the ichnology and infaunal ecology of silurian graptolitic black shales from Sardinia, Italy. Palaeogeogr. Palaeoclimatol. Palaeoecol. 556, 109889 https://doi.org/10.1016/j.palaeo.2020.109889.

Beretka, J., Mathew, P.J., 1985. Natural radioactivity of Australian building materials, industrial wastes and by-products. Health Phys. 48 (1), 87–95. https://doi.org/10.1097/00004032-198501000-00007.

Bochicchio, Francesco, Ampollini, Marco, Antignani, S., Carpentieri, Carmela, Bochicchio, F., Ampollini, M., Carpentieri, C., et al., 2019. Protection from radon in Italy: past, present and perspectives radiation effect enhancement with hyperthermia. Glioblastoma treatment. View project radon survey in Serbia view project protection from radon in Italy: past, present and perspectives. Article in Romanian Journal of Physics 64. https://www.researchgate.net/publication/338117411.

Bossew, Peter, Cinelli, Giorgia, Ciotoli, Giancarlo, Crowley, Quentin G., De Cort, Marc, Elío Medina, Javier, Gruber, Valeria, Petermann, Eric, Tore Tollefsen, 2020. Development of a geogenic radon hazard index—concept, history, experiences. Int. J. Environ. Res. Publ. Health 17 (11), 4134. https://doi.org/10.3390/ijerph17114134.

Carmignani, Luigi, Oggiano, Giacomo, Barca, Sebastiano, Conti, Paolo, Salvadori, Ilio, Eltrudis, Antonio, Funedda, Antonio Luca, Pasci, Sandro, 2001. Geologia Della

Sardegna (Note Illustrative Della Carta Geologica Della Sardegna in Scala 1: 200.000).
Chen, Jing, Rahman, Naureen M., Abu Atiya, Ibrahim, 2010. Radon exhalation from building materials for decorative use. J. Environ. Radioact. 101 (4), 317–322. https://doi.org/10.1016/j.jenvrad.2010.01.005.
Cidu, Rosa, Biddau, Riccardo, Dore, Elisabetta, Vacca, Andrea, Marini, Luigi, 2014. Antimony in the soil–water–plant system at the Su Suergiu abandoned mine (Sardinia, Italy): strategies to mitigate contamination. Sci. Total Environ. 497, 319–331.
Cinelli, Giorgia, Tondeur, Francois, Dehandschutter, Boris, Bossew, Peter, Tore Tollefsen, De Cort, Marc, 2017. Mapping uranium concentration in soil: Belgian experience towards a European map. J. Environ. Radioact. 166 (January), 220–234. https://doi.org/10.1016/j.jenvrad.2016.04.026.
Cocco, Fabrizio, Oggiano, Giacomo, Funedda, Antonio, Loi, Alfredo, Casini, Leonardo, 2018. Stratigraphic, magmatic and structural features of ordovician tectonics in Sardinia (Italy): a review. J. Iber. Geol. 44 (4), 619–639. https://doi.org/10.1007/s41513-018-0075-1.
Cocco, Fabrizio, Loi, Alfredo, Funedda, Antonio, Casini, Leonardo, Ghienne, Jean-François, Pillola, Gian Luigi, Vidal, Muriel, Meloni, Mattia Alessio, Oggiano, Giacomo, 2023. Ordovician tectonics of the south European variscan realm: new insights from Sardinia. Int. J. Earth Sci. 112 (1), 321–344.
Coletti, Chiara, Ciotoli, Giancarlo, Benà, Eleonora, Brattich, Erika, Cinelli, Giorgia, Galgaro, Antonio, Massironi, Matteo, et al., 2022. The assessment of local geological factors for the construction of a geogenic radon potential map using regression kriging. A case study from the euganean hills volcanic district (Italy). Sci. Total Environ. 808 (February), 152064 https://doi.org/10.1016/j.scitotenv.2021.152064.
Corradini, Carlo, Ferretti, Annalisa, 2009. The Silurian of the External Nappes (Southeastern Sardinia).
Cumberland, Susan A., Evans, Katy, Douglas, Grant, de Jonge, Martin, Fisher, Louise, Howard, Daryl, Moreau, John W., 2021. Characterisation of uranium-pyrite associations within organic-rich eocene sediments using EM, XFM-μxanes and μxrd. Ore Geol. Rev. 133, 104051 https://doi.org/10.1016/j.oregeorev.2021.104051.
Darby, S., Hill, D., Auvinen, A., Barros-Dios, J.M., Baysson, H., Bochicchio, F., Deo, H., et al., 2005. Radon in homes and risk of lung cancer: collaborative analysis of individual data from 13 European case-control studies. BMJ 330 (7485), 223. https://doi.org/10.1136/bmj.38308.477650.63.
Dardac, Mirela, Elío, Javier, Aghdam, Mirsina M., Banríon, Méabh, Crowley, Quentin, 2023. Application of airborne geophysical survey data in a logistic regression model to improve the predictive power of geogenic radon maps. A case study in castleisland, county kerry, Ireland. Sci. Total Environ. 894, 164965 https://doi.org/10.1016/j.scitotenv.2023.164965.
Demoury, C., Ielsch, G., Hemon, D., Laurent, O., Laurier, D., Clavel, J., Guillevic, J., 2013. A statistical evaluation of the influence of housing characteristics and geogenic radon potential on indoor radon concentrations in France. J. Environ. Radioact. 126 (December), 216–225. https://doi.org/10.1016/J.JENVRAD.2013.08.006.
Dentoni, Valentina, Da Pelo, Stefania, Mousavi Aghdam, Mirsina, Randaccio, Paolo, Loi, Alfredo, Careddu, Nicola, Bernardini, Alessandra, 2020. Natural radioactivity and radon exhalation rate of Sardinian dimension stones. Construct. Build. Mater. 247 (June), 118377 https://doi.org/10.1016/j.conbuildmat.2020.118377.
East, B.W., 2014. The environmental behaviour of radium, vols 1 and 2. In: International Atomic Energy Agency, Technical Reports Series No. 310, vol. 1989. IAEA, Vienna, 92 0 125190 4.
Erdi-Krausz, G., Matolin, M., Minty, B., Nicolet, J.P., 2003. Guidelines for Radioelement Mapping Using Gamma Ray Spectrometry Data: Also as Open Access E-Book. https://research.utwente.nl/en/publications/guidelines-for-radioelement-mapping-using-gamma-ray-spectrometry-.
Föllmi, K.B., 2012. Early cretaceous life, climate and anoxia. Cretac. Res. 35, 230–257. https://doi.org/10.1016/j.cretres.2011.12.005.
Froňka, A., 2011. Indoor and soil gas radon simultaneous measurements for the purpose of detail analysis of radon entry pathways into houses. Radiat. Protect. Dosim. 145 (2–3), 117–122. https://doi.org/10.1093/rpd/ncr052.
Ghienne, Jean-Francois, Desrochers, André, Vandenbroucke, Thijs R.A., Achab, Aicha, Asselin, Esther, Dabard, Marie-Pierre, Farley, Claude, et al., 2014. A cenozoic-style scenario for the end-ordovician glaciation. Nat. Commun. 5 (1), 4485.
Giustini, Francesca, Ciotoli, Giancarlo, Rinaldini, Alessio, Ruggiero, Livio, Voltaggio, Mario, 2019. Mapping the geogenic radon potential and radon risk by using empirical bayesian kriging regression: a case study from a volcanic area of Central Italy. Sci. Total Environ. 661, 449–464. https://doi.org/10.1016/j.scitotenv.2019.01.146.
Gnoli, Maurizio, Perrier, Vincent, Paolo Serventi, Corradini, C., Ferretti, A., Storch, P., 2009. The state of research on Sardinian silurian Crustacea. The Silurian of Sardinia. Rendiconti Della Societa Paleontologica Italiana 3 (1), 143–155.
Guagliardi, Ilaria, Rovella, Natalia, Apollaro, Carmine, Bloise, Andrea, De Rosa, Rosanna, Scarciglia, Fabio, Buttafuoco, Gabriele, 2016. Effects of source rocks, soil features and climate on natural gamma radioactivity in the crati valley (calabria, southern Italy). Chemosphere 150 (May), 97–108. https://doi.org/10.1016/j.chemosphere.2016.02.011.
Harrell, James A., McKenna, John P., 1993. Report of Investigation n.144. Geological Controls on Indoor Radon in Ohio, Columbus.
Harrell, James A., Belsito, Michael E., Kumar, Ashok, 1991. Radon hazards associated with outcrops of Ohio shale in Ohio. Environ. Geol. Water Sci. 18 (1), 17–26. https://doi.org/10.1007/BF01704574.
Heckel, Philip H., 2008. Pennsylvanian cyclothems in midcontinent north America as far-field effects of waxing and waning of gondwana ice sheets. In: Fielding, C.R., Frank, T.D., Isbell, J.L. (Eds.), Resolving the Late Paleozoic Ice Age in Time and Space, pp. 275–290.
Ishimori, Yuu, Lange, K., Martin, P., Mayya, Y.S., Phaneuf, M., 2013. Measurement and Calculation of Radon Releases from NORM Residues. Iaea.
Kemmer, Gerdi, Keller, Sandro, 2010. Nonlinear least-squares data fitting in excel spreadsheets. Nat. Protoc. 5 (2), 267–281. https://doi.org/10.1038/nprot.2009.182.
Kemski, J., Klingel, R., Siehl, A., Valdivia-Manchego, M., 2009. From radon hazard to risk prediction-based on geological maps, soil gas and indoor measurements in Germany. Environmental Geology 56 (7), 1269–1279. https://doi.org/10.1007/s00254-008-1226-z.
Ketris, M.P., Yudovich, Ya E., 2009. Estimations of clarkes for carbonaceous biolithes: world averages for trace element contents in black shales and coals. Int. J. Coal Geol. 78 (2), 135–148.
Leonardi, F., Bonczyk, M., Nuccetelli, C., Wysocka, M., Michalik, B., Ampollini, M., Tonnarini, S., Rubin, J., Niedbalska, K., Trevisi, R., 2018. A study on natural radioactivity and radon exhalation rate in building materials containing norm residues : preliminary results. Construct. Build. Mater. 173, 172–179. https://doi.org/10.1016/j.conbuildmat.2018.03.254.
Loi, Alfredo, Cocco, Fabrizio, Oggiano, Giacomo, Funedda, Antonio, Vidal, Muriel, Ferretti, Annalisa, Leone, Francesco, et al., 2023. The ordovician of Sardinia (Italy): from the 'sardic phase'to the end-ordovician glaciation, palaeogeography and geodynamic context. Geological Society, London, Special Publications 532 (1), 409–431.
Memarianfard, M., Memarianfard, M., Mousavi Aghdam, M.S., Memarianfard, H., 2016. Health risks zonation in megacities vis-à-vis {PM} using {GIS}-Based model. J. Fund. Appl. Sci. 8 (3), 193. https://doi.org/10.4314/jfas.v8i3s.176.
Mostečak, Ana, Perković, Dario, Kapor, Frankica, Veinović, Želimir, 2018. Radon mapping in Croatia and its relation to geology. Rudarsko-Geolosko-Naftni Zb. 33 (3), 1–11. https://doi.org/10.17794/rgn.2018.3.1.
Olsthoorn, Bart, Rönnqvist, Tryggve, Lau, Cheuk, Rajasekaran, Sanguthevar, Persson, Tomas, Månsson, Martin, Alexander, V., Balatsky, 2022. Indoor radon exposure and its correlation with the radiometric map of uranium in Sweden. Sci. Total Environ. 811 (March), 151406 https://doi.org/10.1016/j.scitotenv.2021.151406.
Örgün, Y., Altinsoy, N., Gültekin, A.H., Karahan, G., Çelebi, N., 2005. Natural radioactivity levels in granitic plutons and groundwaters in southeast part of eskisehir, Turkey. Appl. Radiat. Isot. 63 (2), 267–275. https://doi.org/10.1016/j.apradiso.2005.03.008.
Pearson, Karl, 1895. VII. Note on regression and inheritance in the case of two parents. Proc. Roy. Soc. Lond. 58 (347–352), 240–242.
Pereira, A.J.S.C., Neves, L.J.P.F., 2012. Estimation of the radiological background and dose assessment in areas with naturally occurring uranium geochemical anomalies—a case study in the iberian massif (Central Portugal). J. Environ. Radioact. 112, 96–107. https://doi.org/10.1016/j.jenvrad.2012.05.022.
Perry, S.A., I Marcellus Shale Team, P.R., 2011. Understanding naturally occurring radioactive material in the marcellus shale. Marcellus Shale 1–8.
RAS, 2013. Carta Geologica Di Base Della Sardegna in Scala 1: 25000. Regione Autonoma della Sardegna.
Sadrnejhad, Amirodin, Seyed, Mousavi Aghdam, Mir Sina, MemarianFard, Mahsa, Tehrani, Zahra Sharif, 2016. Geothermal heat store in unsaturated/saturated soil charged from a solar heating system. International Journal Of Geo Science and Environmental Planning 1 (2), 1–10.
Sahoo, B.K., Mayya, Y.S., 2010. Two dimensional diffusion theory of trace gas emission into soil chambers for flux measurements. Agric. For. Meteorol. 150 (9), 1211–1224. https://doi.org/10.1016/j.agrformet.2010.05.009.
Schön, Jürgen H., 2015. Physical Properties of Rocks: Fundamentals and Principles of Petrophysics. Elsevier.
Soesoo, A., Hade, S., 2014. Black shale of estoni: moving towards a fennoscandian-baltoscandian database. Труды Карельского Научного Центра РАН 1, 103–114.
Swanson, Vernon Emanuel, 1961. Geology and Geochemistry of Uranium in Marine Black Shales: A Review. US Government Printing Office, Washington, DC.
Tan, Yanliang, Xiao, Detao, 2011. Revision for measuring the radon exhalation rate from the medium surface. IEEE Trans. Nucl. Sci. 58 (1), 209–213. https://doi.org/10.1109/TNS.2010.2090897, 2.
Thu, Huynh Nguyen Phong, Van Thang, Nguyen, Hong Loan, Truong Thi, Van Dong, Nguyen, others, 2019. Natural radioactivity and radon emanation coefficient in the soil of ninh son region, vietnam. Appl. Geochem. 104, 176–183.
Tondeur, François, Cinelli, Giorgia, Dehandschutter, Boris, 2014. Homogenity of Geological Units with Respect to the Radon Risk in the Walloon Region of Belgium" 136: 140–51.
UNSCEAR, 2008. Effects of Ionizing Radiation: Report to the General Assembly, with Scientific Annexes, vol. 1. United Nations Publications.
Yarmoshenko, I., Vasilyev, A., Malinovsky, G., Bossew, P., Žunić, Z.S., Onischenko, A., Zhukovsky, M., 2016. Variance of indoor radon concentration: major influencing factors. Sci. Total Environ. 541 (January), 155–160. https://doi.org/10.1016/J.SCITOTENV.2015.09.077.
Zanin, Yu N., Zamirailova, A.G., Eder, V.G., 2016. Uranium, thorium, and potassium in black shales of the Bazhenov formation of the west Siberian marine basin. Lithol. Miner. Resour. 51 (1), 74–85.
Zeeb, Hajo, Shannoun, Ferid, World Health Organization, 2009. WHO Handbook on Indoor Radon: A Public Health Perspective. World Health Organization.